Correlation of Structure and Morphology in an Ethylene-glycol Side-chain Modified Polythiophene via Combined X-ray Scattering and Four-dimensional Scanning Transmission Electron Microscopy

A. Herzing, R. Li

To be published in "Small Methods"

January 2025

DISCLAIMER

Correlation of Structure and Morphology in an Ethylene-glycol Side-chain Modified Polythiophene via Combined X-ray Scattering and Four-dimensional Scanning Transmission Electron Microscopy

Andrew A. Herzing,[*,†] Lucas Q. Flagg,[†] Lee J. Richter,[†] Jonathan W. Onorato,[‡]
Christine K. Luscombe,[¶] and Ruipeng Li[§]

†*Material Measurement Laboratory, National Institute of Standards and Technology, Gaithersburg, MD 20872, USA*

‡*Department of Materials Science and Engineering, University of Washington, Seattle, Washington 98195, USA*

¶*pi-Conjugated Polymer Unit, Okinawa Institute of Science and Technology Graduate University, 1919-1 Tanacha, Onna-son, Kunigami-gun, Okinawa, 904-0495, Japan*

§*National Synchrotron Light Source II, Brookhaven National Laboratory, Upton, NY 11973, USA*

E-mail: andrew.herzing@nist.gov

Abstract

We report the results of a combined grazing incidence wide-angle X-ray scattering (GIWAXS) and four-dimensional scanning transmission microscopy (4D-STEM) analysis the effects of thermal processing on poly(3[2-(2-methoxyethoxy)ethoxy]methylthiophene-

2,5-diyl), a conjugated semiconducting polymer used as the active layer in organic electrochemical transistor devices. GIWAXS provides a measure of overall crystallinity in the film, while 4D-STEM produces real-space maps of the morphology and orientation of individual crystals along with their spatial extent and distribution. The sensitivity of the 4D-STEM detector allows for collection of full electron diffraction patterns at each position in an image scan while limiting the imparted electron dose to below the damage threshold. The effects of heat treatment on the distribution and type of crystals present in the films is determined.

Introduction

Conjugated semiconducting polymers are being widely studied for their application in a host of new technologies. For bioelectronic applications, organic electrochemical transistors (OECTs) show great promise due to their unique match to the mechanical properties of tissue and their mixed ionic and electronic conduction.[1–4] In an OECT, an active polymer layer is patterned with source/drain electrodes on the underside, while the top surface is in contact with an electrolyte solution. When an electrical bias is applied to the solution via a gate electrode, ions from the solution are driven into the polymer in an electrochemical doping process. The result is a change in conductivity of the polymer layer which can be monitored by measuring the current flow between the source and drain. For an p-type accumulation mode device, charge transport is minimal in the undoped state due to the lack of mobile carriers (holes). When the polymer is immersed in the electrolyte solution, the film swells as it absorbs liquid. Upon the application of electrical bias, holes are injected into the film from the bottom electrode and this charge is compensated by the uptake of ions from solution further swelling the film. Increasing the bias voltage increases the concentration of ions in the film along with the degree of film swelling. Unlike a field-gated thin-film transistor (TFT), the conductance of the active layer in an OECT is controlled by electrochemical doping of the entire volume of active material. This can involve significant changes in the active layer structure due to the ingress of electrolyte and counter ions. Further structural changes may also occur as a result of the high induced carrier density.[5]

Much progress has been made in the development of new, optimized materials for these applications. In particular, the introduction of polar side-chain species to the backbone of OECT polymers has been shown to facilitate the uptake of ions from the aqueous electrolyte at reasonable potentials.[6] In TFTs, it is well established that electrical performance can be extremely sensitive to the detailed microstructure that is a function of both casting conditions and subsequent thermal processing.[7–10] Strikingly, very little work has been done in studying the role of film processing of the materials being developed for OECTs. It can be anticipated that behavior will be more complex, due to trade-offs between ion uptake and electronic mobility. For example, in one recent study, OECTs with increased crystallinity were shown to exhibit decreased performance.[11] There has been speculation that this behavior can be attributed to the preferential swelling of the amorphous region of the film, however this is difficult to measure experimentally. Moving forward, the ability to spatially resolve the crystalline domains of the polymer is essential to understanding the role of crystallinity and nanoscale morphology on the performance of OECT materials, and therefore enable the design of better OECT materials and processing conditions.

Scanning transmission electron microscopy (STEM) is ideally suited to simultaneously reveal the morphological and structural characteristics of materials organized at nanometer length scales and below. One particularly powerful technique available in the STEM is known as scanning nanobeam diffraction or four-dimensional (4D)-STEM. In this technique, a full two-dimensional electron scattering pattern is collected at every point in a two-dimensional image scan such that the variations in crystallinity and orientation can be measured at nanometer spatial resolutions. Of particular relevance to the present work, Panova *et al.*[12] recently employed 4D-STEM to map the crystalline orientation in a copolymer blend of semi-crystalline poly(3-hexylthiophene-2,5-diyl) (P3HT) and amorphous polystyrene. More recently, the same group reported results from thin films of poly[2,5-bis(3-

tetradecylthiophen-2-yl)thieno[3,2-b]thiophene] (PBTTT) and a small-molecule material.[13] The methods employed in these preceding studies cannot be applied to many organic materials due to the elevated electron doses employed (tens of thousands of electrons per square nanometer) as the high-energy electron beam rapidly destroys the crystal structure and can even completely vaporize material at elevated dose.[14] The development of high-sensitivity, direct electron detectors offer a way of surmounting this barrier, as the required data can be collected with a far lower electron dose than required using CCD-based cameras.[15,16] Most recently, a modified optical approach to 4D-STEM has even enabled the analysis of dynamic structural changes in a polymer film during heat treatment.[17]

In this paper we discuss the application of 4D-STEM to the characterization of a state of the art OECT material: poly(3[2-(2-methoxyethoxy) ethoxy]methylthiophene-2,5-diyl) (P3MEEMT).[11,18,19] P3MEEMT (see Fig.1(a) contains ethylene glycol-based side chains for enhanced ion uptake and exhibits carrier mobilities comparable to state-of-the-art OECT's. We will demonstrate the utility of 4D-STEM for tracking the structural changes with heat treatment in this material.

Results and discussion

GIWAXS

Grazing incidence wide-angle X-ray scattering (GIWAXS) measurements were performed in order to assess the crystallinity in the P3MEEMT films and the evolution of the film morphology and structure with thermal annealing. The patterns obtained from as cast and annealed films are presented in Figures 2(a-e). The evident lamellar crystal structure is similar to those observed from other, more widely studied thiophene derivatives such as P3HT; however, the rich evolution with annealing temperature is distinctive. In these patterns, out of plane scattering is indicated along the y-axis while the in-plane scattering occurs along the x-axis. The (100) diffraction from the inter-lamellar repeat occurs at $q \approx$

3.3 nm^{-1} and the (010) diffraction from the $\pi - \pi$ stacking occurs at approximately 17.0 nm^{-1}. These values correspond to a lamellar repeat distance of 1.9 nm and a $\pi - \pi$ stacking distance of 0.4 nm. The former value is somewhat larger than reported for P3HT owing to the longer side chain species present in P3MEEMT.

The GIWAXS data show that the as-cast film exhibits little order as the pattern contains only broad, diffuse features. A strong (100) peak is observed upon annealing at 75 °C with pronounced intensity peaks in both the in-plane and out-of-plane orientations. The (200) and (300) peaks can alse be seen in the in-plane orientation, indicating a high degree of order within the crystals. The (100) peak reaches the maximum observed intensity at annealing temperatures of 115 °C and 145 °C before returning to the disordered state at 175 °C. Differential scanning calorimetry reveals an upper melting/clearing temperature of $\approx$ 155 °C (Figure S1). The (010) peak intensity is more difficult to track quantitatively since it is positioned at a point in reciprocal space where it overlaps the broad amorphous scattering from the side chains and the background due to the underlying support in a complex manner. However, it can be qualitatively seen that the (010) intensity increases in both the in-plane and out-of-plane orientations with annealing temperature up to 145 °C before decreasing back to a similar value as was observed in the as-cast film. Quantitatively, the crystal orientation distributions (Figure S2 (100) pole figure), crystal quality (Table S1 coherence length and paracrystallinity), and relative crystallinity (Figure S3) all evolve significantly with temperature.

For the purposes of comparing this data to our subsequent 4DSTEM analysis, only the in-plane scattering, nearest the horizon, is relevant, while in GIWAXS, nearly the entire pole-figure (the beam-specimen orientation) is captured in the 2D pattern. Angular sampling is limited in 4D-STEM; especially for soft organic materials where only a single scan is feasible before structural alteration has occurred. Consequently, 4D-STEM will only be sensitive to those crystals which are oriented at the Bragg angle with respect to the electron beam. When the beam is parallel to the surface normal of the film, as it is in all cases presented in this paper, the primary reflections arise from the in-plane crystal repeat orientations. In-plane crystals in P3MEEMT thin films can be present in either a face-on or edge-on orientation. In face-on oriented crystals, the (100) inter-lamellar repeat is parallel to the substrate surface (*i.e.* in-plane) while the $\pi - \pi$ repeat is parallel to the substrate surface normal (*i.e.* out-of-plane). For edge-on oriented crystals, the orientation of the two crystal repeats is reversed with respect to the substrate. These two crystal orientations are shown schematically in Figures 1(b and c).Appropriate in-plane line-cuts of the GIWAXS patterns are shown in Figure 2f.

Diffraction Features in 4D-STEM

Turning to the 4D-STEM data, we first focus on data from a film annealed at 115 °C, a temperature at which in-plane crystallinity has been maximized. This data can be inspected in a variety of ways. Most simply, the integrated diffraction data from all scan locations is shown in Figure 3. While some clear differences can be seen, such as sharpening of the high q ring at 17 nm^{-1} upon moderate anneals, they are difficult to interpret since the diffracted features are diluted by the contribution from the amorphous phase. When the individual patterns are examined, three primary types of diffraction patterns were found and an example of each is shown in Figure 4. Patterns collected from many specimen locations do not show any strong diffracted intensity. Instead, only a weakly diffuse background decaying continuously from q=0 is observed. The material at these locations is either non-crystalline or is not oriented in the diffraction condition. The background in these experiments is very small since the beam energy (200 keV) is large and the film thickness ($\approx$ 50 nm - 80 nm) is small. Outside of these amorphous areas, a large number of pixels show strong diffracted intensity at $q \approx 3.3$ nm^{-1}. This is the (100) reflection and indicates the presence of a face-on oriented crystal at these pixel locations. Often in these pixels, second and third order diffraction peaks with symmetric intensity are also observed, suggesting that the crystal quality in these domains is very high and that their orientation is at or very near the Bragg angle. A small minority of pixels where the (100) reflection was observed contained a second set of (100) reflections at a different orientation. This indicates that the beam is sampling two crystals in the same pixel which are either laterally or vertically adjacent. Finally, a second population of crystals was observed which showed weaker diffracted intensity at $q \approx$ 17.0 nm^{-1}, corresponding to the (010) $\pi - \pi$ stacking in edge-on orientation crystals. These are spatially distinct from the face-on crystals.

Virtual Images and Crystal Orientation

The spatial distribution of crystals in the film can be directly visualized by extracting virtual images from the 4D-STEM data. This is accomplished by applying an annular mask over the chosen scattering range and integrating the total diffracted intensity (Fig. 5). The resulting 2D real space image is a map of those regions of the specimen that contribute strongly to this particular diffracted intensity. When this is done for the (100) diffraction signal, a population of (40 to 50) nm long crystalline domains is revealed.

Since the 4D-STEM data affords us a simultaneous view of the real space crystal morphology and the reciprocal space structural information, we can unambiguously determine the orientational relationship between the lattice repeat and the crystal growth direction. Our analysis indicates that the (100) crystals are elongated in the direction parallel to the crystalline planes giving rise to the diffraction discs. This is demonstrated in Figure 6 which shows several patterns extracted from (100) oriented crystals in the sample annealed at 115 °C. The diffraction vector in each pattern (*i.e.* the vector from the central, transmitted spot to the diffracted spots) is parallel to the long axis of the corresponding crystal in the real space image. Note that the orientational relationship between the beam scan/real space images and the detector/diffraction patterns must be properly configured since the beam scan direction can be freely rotated while the detector is fixed (see the Experimental Methods section). The (40 to 50) nm length along the (100) direction of the observed crystals is consistent with the GIWAXS coherence length of the in-plane population, determined to be

35 ± 10 nm (Table S1). GIWAXS cannot inform on the relatively narrow length along the (001) direction, as no (001) diffraction features are visible.

By locating the diffraction peaks in all patterns associated with (100) crystals and determining their relative angle, the orientational distribution of crystals can be assessed. As shown in Figure 7, the orientation of the face on crystals varies continuously as would be expected for a spin cast film of this kind. The lower diffracted intensity of the higher-q, edge-on crystals makes this type of analysis infeasible, but there is no reason to expect an orientation preference of these crystals when none is observed in their face-on counterpart.

Effect of Heat Treatment Temperature

4D-STEM datasets were collected using identical conditions from a series of films annealed at 75 °C, 115 °C, 145 °C, and 175 °C. Example diffraction patterns extracted from pixels associated with (100) and (010) oriented crystals for each heat treatment condition are shown in Figure 8. These patterns were located in the 4D-STEM dataset by locating the most intense pixels in the (100) and (010) virtual images. Patterns from an unannealed, as-cast film (not shown) showed no strong diffraction peaks whatsoever. This is expected in P3MEEMT where GIWAXS analysis has indicated that appreciable crystal formation does not occur until heat treatment has been applied. Upon heating to 75 °C, some faint traces of (100) diffraction peaks begin to appear, while the (010) peak is not observed. Further heat treatment at 115 °C promotes the increased ordering in the (100) crystals, where the diffraction peak intensities is much higher than at 75 °C and where second and third order reflections are observed. The 115 °C treatment also promotes the formation of edge-on (010) oriented crystals whose diffraction peaks are less intense then those associated with the (100) crystals. Similar features are observed in the patterns and virtual images from the film annealed at 145 °C as were seen in the 115 °C film. Finally, the patterns extracted from the 175 °C dataset show no strong diffraction features. These patterns and the trends in crystallinity they indicate are also shown as 1D radially integrated plots in Figure 9. These plots were produced by taking the average of the 50 most intense pixels in the (100) and (010) virtual images and therefore show superior signal above background than the individual patterns shown previously. Because of this, it can be seen that there is a small amount of (100) diffracted intensity in the film annealed at 175 °C. This temperature is above the P3MEEMT melting point, thus this film is melt-recrystallized and the minor crystallinity indicates kinetic constraints to re-crystallization during the nominal quench (free cooled in N_2 upon removal from the hot plate). Overall, the crystal-selected 4D-STEM diffraction patterns (Figure 9) are in striking agreement with the in-plane GIWAXS patterns (Figure 2f). The real space distribution of the (100) and (010) crystals is shown in the associated virtual images collected in Figure 10. The trend here matches that already described in the X-ray diffraction data. For the (100) images, we can see the formation of poorly ordered crystals at 75 °C, enhanced crystallinity at 115 °C and 145 °C, and loss of aggregated crystallinity at 175 °C. In the case of the (010) images, discrete crystals are only observed above 115 °C. Of particular note is the formation of much smaller crystals upon recrystallization from the melt, as evidenced in both the 4D-STEM (Figure 10) and the coherence length (Table S1).

Conclusions

The combined GIWAXS and 4D-STEM characterization has revealed a complex, non-monotonic, behavior for P3MEEMT as a function of thermal processing. Crystallinity was found to increase with annealing temperature up to 145 °C before decaying back to a disordered state when annealed above the melt (175 °C). The crystals that formed upon annealing were observed to be (40 to 50) nm in length with a lamellar packing orientation was found to be parallel to the long axis of the crystals. The orientation distribution of the in-plane crystals was found to be isotropic. The combination of reciprocal space structural detail and real space visualization of the crystals could prove to be a valuable tool for diagnosing the role of crystallinity in OECT performance going forward. Further, it may be useful for extending our understanding of the swelling of amorphous material upon electrochemical doping which is hypothesized to cause crystallite separation and disruption of charge conduction pathways.

Experimental Section

Materials and Sample Preparation

P3MEEMT, was synthesized as described previously.[11] Based on high performance liquid chromatography, the number average molar mass (Mn) was 23 kg/mol with dispersity, Mw/Mn, of 1.88. Substrates were cleaned by 10 min ultrasonic agitation in each of chloroform and isopropyl alcohol, followed by ultraviolet-ozone treatment for 10 min. P3MEEMT was deposited by blade coating with a custom, low angle coater.[20] The blade height was 200 μm and the blade speed nominally 40 mm/s. Substrate temperature was 30 °C. Blade speed was varied to produce variable film thickness. The solution was 20 mg/mL in chlorobenzene. Solution was dissolved at 50 °C with stirring and allowed to cool to room temperature. Typical film thickness was 75 nm.

Samples were prepared for TEM analysis by first blade coating a film of 23 kDa P3MEEMT onto a sacrificial Na:polystyrene sulfonate layer supported on a glass substrate. Next, the films were delaminated in deionized water and picked up using a silicon nitride TEM membrane. The nitride membrane was necessary to carry out heat treatments at elevated temperature, as the P3MEEMT melt transition occurs at $\approx$ 152 °C and the films were observed to rupture upon annealing when supported on a traditional copper TEM grid. Heat treatments were performed using a hot plate by placing the grid or membrane directly onto the heated surface for twenty minutes in a nitrogen atmosphere. Samples were made using annealing temperatures of 75 °C, 115 °C, 145 °C, and 175 °C. For GIWAXS, films were directly deposited on a clean Si wafer.

GIWAXS

Scattering experiments were performed at the CMS BM-11 beam-line in the NSLS-II at the Brookhaven National Laboratory, NY, USA. GIWAXS patterns were collected with a Pilatus 2D detector by irradiating samples with 13.5 keV X-rays at a nominal 250 mm distance in a vacuum environment. Data were treated and corrected with the NIKA software package[21] within IgorPro environment. GIWAXS patterns were calibrated with a silver behenate sample.

STEM Analysis

4D-STEM data was collected using an FEI Titan 80-300 TEM/STEM operating at 200 keV. The dose response of P3MEEMT films was characterized by collecting a series of 4D-STEM datasets from the same region of the specimen annealed at 115 °C. In order to monitor any structural changes with increasing electron dose, a very low probe current was employed for these measurements. The probe current was measured using a calibrated picoammeter attached to the fluorescent screen of the microscope. The probe currents employed were quite low ($\approx$ 5 pA) making their absolute measurement difficult. However, the measurement is consistent over time making it adequate for determining the instrument parameters for analysis. Patterns collected in this way are shown as a function of electron dose in supplementary Figure S1. Two series are shown, one where the dose per frame was quite low (top row) and another where the dose per frame was increased by holding the probe current constant but increasing the frame acquisition time by a factor of five. Radial integration of the data from the lower dose series is shown in Figure S2. It is evident from this data that the (100) crystals are more robust to electron bombardment than the (010) crystals. Both types of crystals can be analyzed by limiting the dose to below 1800 e^{-}/nm^{2}.

A small 5 um probe-forming aperture was used resulting in a probe current of approximately (10 to 30) pA. This aperture is included as part of a custom chip designed by Molecular Foundry[22,23] and results in a probe convergence semi-angle of $\approx$ 0.3 mrad and a focused probe size of $\approx$ 10 nm FWHM. The small convergence ensures separation of the Bragg diffraction discs as well as more strongly peaked diffraction features. A Quantum Detectors Merlin direct detection camera with a 256 pixel x 256 pixel array was used to collect the electron scattering patterns using a readout time of (1 - 5) msec per pixel with a spatial sampling of 16 nm. Data processing was performed using the FPD Python package[24,25] along with custom scripts developed for this application.[26]

Virtual Image Formation and Diffraction Pattern Extraction

The center of each pattern was determined by a center of mass analysis. To form dark field virtual images, annular reciprocal space masks were created which were centered at $q = (0, 0)$ and surrounded the q scattering value for either the (100) or (010) reflections. The masks were applied to each diffraction pattern in the 4D dataset and the remaining intensity was integrated resulting in a 2D array representing the scattered intensity at each scan pixel. Virtual bright field images were formed in a similar fashion except using circular masks centered at $q = (0, 0)$.

Diffraction patterns associated with each crystal type were extracted by locating the pixels in the (100) and (010) dark field images which showed the greatest intensity.

Crystal Orientation Determination

The orientation of the beam scan with respect to the detector must be properly set so that the reciprocal space scattering directions can be directly related to the real space features. Our detector is oriented at approximately 90° from the slow scan direction of the beam when no scan rotation is applied. To correct this, a 90° rotation is applied to the beam scan and the rotation is finely adjust by viewing the scan raster on the detector to ensure that the scan proceeds from top to bottom and left to right on the 4D-STEM detector.

A crystal orientation map of the film annealed at 115 °C was produced by first masking the data in real space using a binarized version of the (100) virtual image. The threshold for binarization was determined using Otsu's method.[27] Then, the diffraction pattern in each masked pixel was limited to the (100) q range by application of an annular reciprocal space mask centered on the patterns center of mass. Finally, peak locations were determined using a 2D local maxima detection algorithm on the masked patterns and calculating the inverse tangent of the vector connecting the center of the pattern to the diffraction peak.

Disclaimer

Trade names and commercial products are identified in this paper to specify the experimental procedures in adequate detail. This identification does not imply recommendation or endorsement by the authors or by the National Institute of Standards and Technology, nor does it imply that the products identified are necessarily the best available for the purpose. The authors declare no competing financial interest.

Acknowledgement

Work at the Molecular Foundry was supported by the Office of Science, Office of Basic Energy Sciences, of the U.S. Department of Energy under Contract No. DE-AC02-05CH11231.

Andrew Herzing thanks Meghan Holtz for determining the optimized parameters for the 4D-STEM detector.

This research used beamline 11-BM (CMS) of the National Synchrotron Light Source, a U.S. Department of Energy (DOE) Office of Science User Facility operated for the DOE Office of Science by Brookhaven National Laboratory under contract no. DE-SC0012704.

Supporting Information Available

The following files are available free of charge.

- Herzing-4DSTEM-OECT_SI.pdf: 4DSTEM dose analysis results from P3MEEMT.

- All data and Jupyter notebook of data processing is available online.

References

(1) Rivnay, J.; Inal, S.; Salleo, A.; Owens, R. M.; Berggren, M.; Malliaras, G. G. Organic electrochemical transistors. *Nature Reviews Materials* **2018**, *3*, 17086.

(2) Malliaras, G.; McCulloch, I. Introduction: Organic Bioelectronics. *Chemical Reviews* **2022**, *122*, 4323–4324, Publisher: American Chemical Society.

(3) Koklu, A.; Ohayon, D.; Wustoni, S.; Druet, V.; Saleh, A.; Inal, S. Organic Bioelectronic Devices for Metabolite Sensing. *Chemical Reviews* **2022**, *122*, 4581–4635, Publisher: American Chemical Society.

(4) Pitsalidis, C.; Pappa, A.-M.; Boys, A. J.; Fu, Y.; Moysidou, C.-M.; van Niekerk, D.; Saez, J.; Savva, A.; Iandolo, D.; Owens, R. M. Organic Bioelectronics for In Vitro Systems. *Chemical Reviews* **2022**, *122*, 4700–4790, Publisher: American Chemical Society.

(5) LeCroy, G.; Cendra, C.; J. Quill, T.; Moser, M.; Hallani, R.; F. Ponder, J.; Stone, K.; D. Kang, S.; Yu-Lun Liang, A.; Thiburce, Q.; McCulloch, I.; C. Spano, F.; Giovannitti, A.; Salleo, A. Role of aggregates and microstructure of mixed-ionic–electronic-conductors on charge transport in electrochemical transistors. Publisher: Royal Society of Chemistry.

(6) Giovannitti, A.; Sbircea, D.-T.; Inal, S.; Nielsen, C. B.; Bandiello, E.; Hanifi, D. A.; Sessolo, M.; Malliaras, G. G.; McCulloch, I.; Rivnay, J. Controlling the mode of operation of organic transistors through side-chain engineering. *Proceedings of the National Academy of Sciences* **2016**, *113*, 12017–12022.

(7) Chang, J.-F.; Sun, B.; Breiby, D. W.; Nielsen, M. M.; Sölling, T. I.; Giles, M.; McCulloch, I.; Sirringhaus, H. Enhanced Mobility of Poly(3-hexylthiophene) Transistors by

Spin-Coating from High-Boiling-Point Solvents. *16*, 4772–4776, Publisher: American Chemical Society.

(8) McCulloch, I.; Heeney, M.; Bailey, C.; Genevicius, K.; MacDonald, I.; Shkunov, M.; Sparrowe, D.; Tierney, S.; Wagner, R.; Zhang, W.; Chabinyc, M. L.; Kline, R. J.; McGehee, M. D.; Toney, M. F. Liquid-crystalline semiconducting polymers with high charge-carrier mobility. *5*, 328–333, Number: 4 Publisher: Nature Publishing Group.

(9) Salleo, A.; Kline, R. J.; DeLongchamp, D. M.; Chabinyc, M. L. Microstructural Characterization and Charge Transport in Thin Films of Conjugated Polymers. *22*, 3812–3838, _eprint: https://onlinelibrary.wiley.com/doi/pdf/10.1002/adma.200903712.

(10) Zen, A.; Pflaum, J.; Hirschmann, S.; Zhuang, W.; Jaiser, F.; Asawapirom, U.; Rabe, J. P.; Scherf, U.; Neher, D. Effect of Molecular Weight and Annealing of Poly(3-hexylthiophene)s on the Performance of Organic Field-Effect Transistors. *14*, 757–764, _eprint: https://onlinelibrary.wiley.com/doi/pdf/10.1002/adfm.200400017.

(11) Flagg, L. Q.; Bischak, C. G.; Onorato, J. W.; Rashid, R. B.; Luscombe, C. K.; Ginger, D. S. Polymer Crystallinity Controls Water Uptake in Glycol Side-Chain Polymer Organic Electrochemical Transistors. *Journal of the American Chemical Society* **2019**, *141*, 4345–4354.

(12) Panova, O.; Chen, X. C.; Bustillo, K. C.; Ophus, C.; Bhatt, M. P.; Balsara, N.; Minor, A. M. Orientation mapping of semicrystalline polymers using scanning electron nanobeam diffraction. *Micron* **2016**, *88*, 30–36.

(13) Panova, O.; Ophus, C.; Takacs, C. J.; Bustillo, K. C.; Balhorn, L.; Salleo, A.; Balsara, N.; Minor, A. M. Diffraction imaging of nanocrystalline structures in organic semiconductor molecular thin films. *Nature Materials* **2019**, *18*, 860–865.

(14) Egerton, R. F.; Li, P.; Malac, M. Radiation damage in the TEM and SEM. *Micron* **2004**, *35*, 399–409.

(15) Ophus, C. Four-Dimensional Scanning Transmission Electron Microscopy (4D-STEM): From Scanning Nanodiffraction to Ptychography and Beyond. *Microscopy and Microanalysis* **2019**, *25*, 563–582.

(16) Bustillo, K. C.; Zeltmann, S. E.; Chen, M.; Donohue, J.; Ciston, J.; Ophus, C.; Minor, A. M. 4D-STEM of Beam-Sensitive Materials. *Accounts of Chemical Research* **2021**, *54*, 2543–2551.

(17) Wu, M.; Harreiß, C.; Ophus, C.; Johnson, M.; Fink, R. H.; Spiecker, E. Seeing the Structure and Structural Evolution of Nano-crystallites in Soft Materials Using 4D Scanning Confocal Electron Diffraction. *Microscopy and Microanalysis* **2022**, *28*, 464–466, Publisher: Cambridge University Press.

(18) Dong, B. X.; Nowak, C.; Onorato, J. W.; Strzalka, J.; Escobedo, F. A.; Luscombe, C. K.; Nealey, P. F.; Patel, S. N. Influence of Side-Chain Chemistry on Structure and Ionic Conduction Characteristics of Polythiophene Derivatives: A Computational and Experimental Study. *Chemistry of Materials* **2019**, *31*, 1418–1429.

(19) Flagg, L. Q.; Bischak, C. G.; Quezada, R. J.; Onorato, J. W.; Luscombe, C. K.; Ginger, D. S. P-Type Electrochemical Doping Can Occur by Cation Expulsion in a High-Performing Polymer for Organic Electrochemical Transistors. *ACS Materials Letters* **2020**, *2*, 254–260.

(20) Stafford, C. M.; Roskov, K. E.; Epps, T. H.; Fasolka, M. J. Generating thickness gradients of thin polymer films via flow coating. *Review of Scientific Instruments* **2006**, *77*, 023908, Publisher: American Institute of Physics.

(21) Ilavsky, J. *Nika* : software for two-dimensional data reduction. *Journal of Applied Crystallography* **2012**, *45*, 324–328.

(22) Zeltmann, S. E.; Müller, A.; Bustillo, K. C.; Savitzky, B.; Hughes, L.; Minor, A. M.;

Ophus, C. Patterned probes for high precision 4D-STEM bragg measurements. *Ultramicroscopy* **2020**, *209*, 112890.

(23) Mahr, C.; Müller-Caspary, K.; Grieb, T.; Krause, F. F.; Schowalter, M.; Rosenauer, A. Accurate measurement of strain at interfaces in 4D-STEM: A comparison of various methods. *Ultramicroscopy* **2021**, *221*, 113196.

(24) Nord, M.; Webster, R. W. H.; Paton, K. A.; McVitie, S.; McGrouther, D.; MacLaren, I.; Paterson, G. W. Fast Pixelated Detectors in Scanning Transmission Electron Microscopy. Part I: Data Acquisition, Live Processing, and Storage. *Microscopy and Microanalysis* **2020**, *26*, 653–666.

(25) Paterson, G. W.; Webster, R. W. H.; Ross, A.; Paton, K. A.; Macgregor, T. A.; McGrouther, D.; MacLaren, I.; Nord, M. Fast Pixelated Detectors in Scanning Transmission Electron Microscopy. Part II: Post-Acquisition Data Processing, Visualization, and Structural Characterization. *Microscopy and Microanalysis* **2020**, *26*, 944–963.

(26) Herzing, A. A. MerlinTools. 2021; `https://github.com/AndrewHerzing/merlintools`.

(27) Otsu, N. A Threshold Selection Method from Gray-Level Histograms. *IEEE Transactions on Systems, Man, and Cybernetics* **1979**, *9*, 62–66.

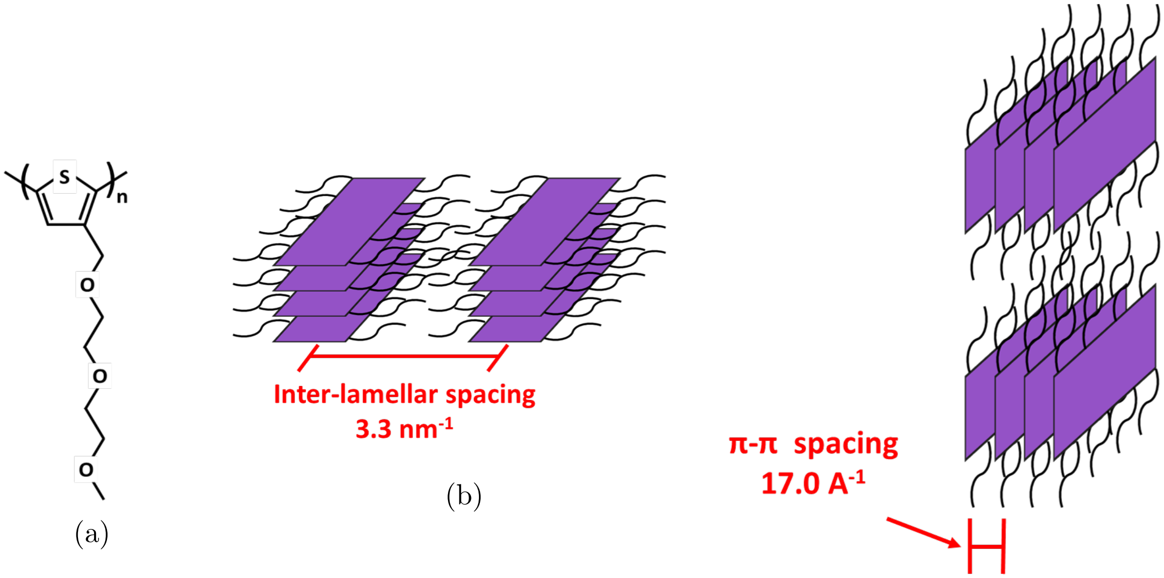

(a)

(b)

(c)

Figure 1: Chemical structure of P3MEEMT (left) along with schematic depictions of the in-plane lamellar repeat distances expected from GIWAXS analysis. Face-on stacking (middle, expected in-plane q = 3.3 nm^{-1}) and edge-on stacking (right, expected in-plane q = 17.0 nm^{-1})

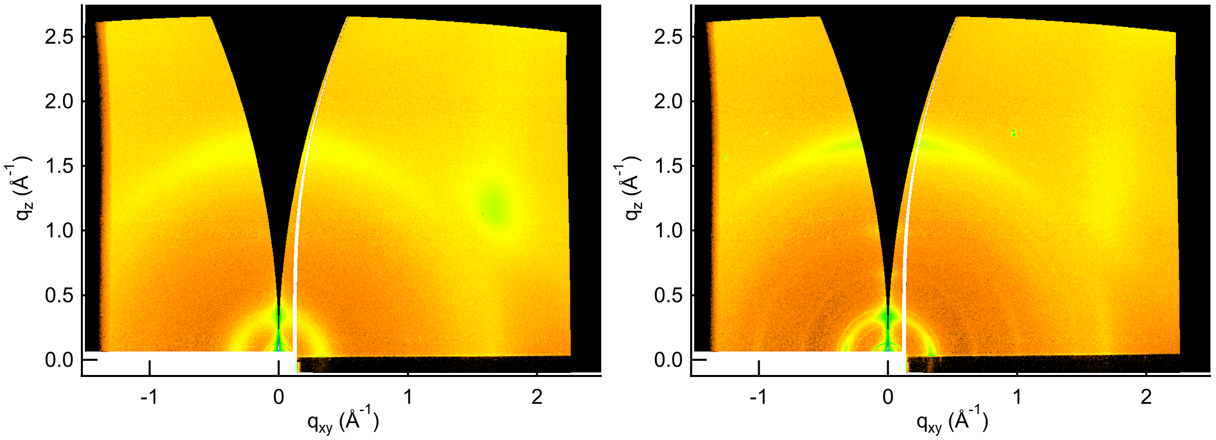

(a) As Cast (b) 75 °C

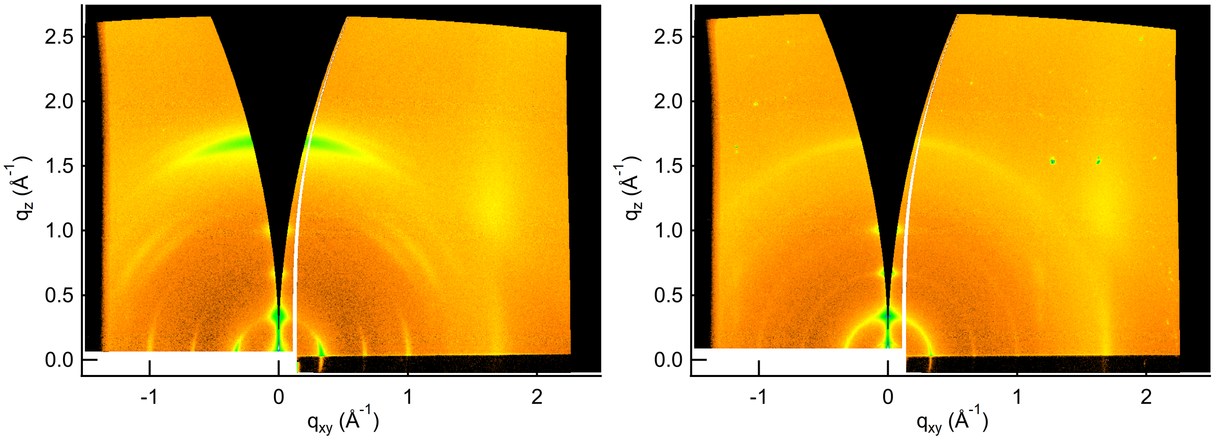

(c) 115 °C (d) 145 °C

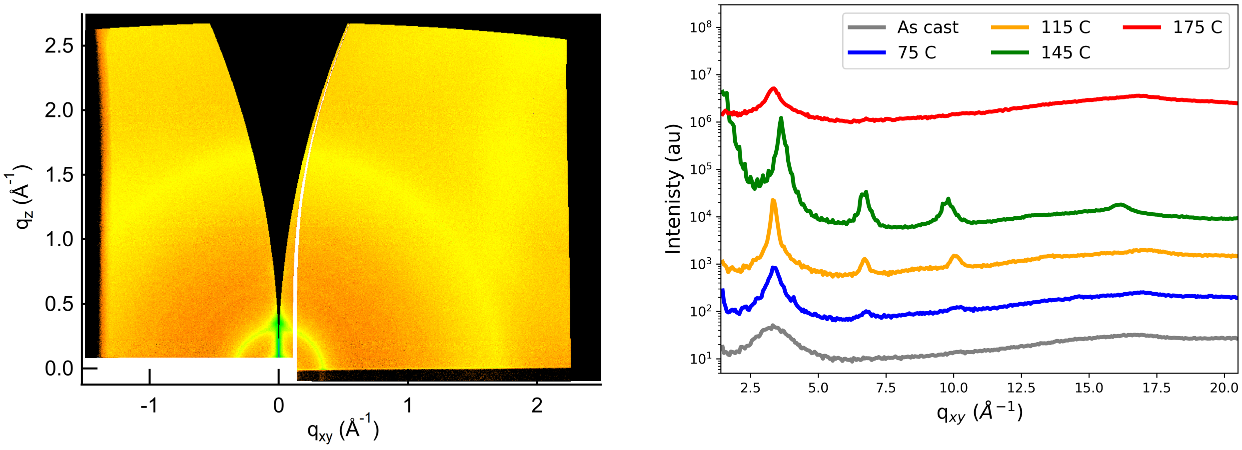

(e) 175 °C (f)

Figure 2: GIWAXS patterns (a-e) collected from the P3MEEMT thermal annealing series. Also shown is a plot of the intensity along the in-plane direction (x-axis) only (f).

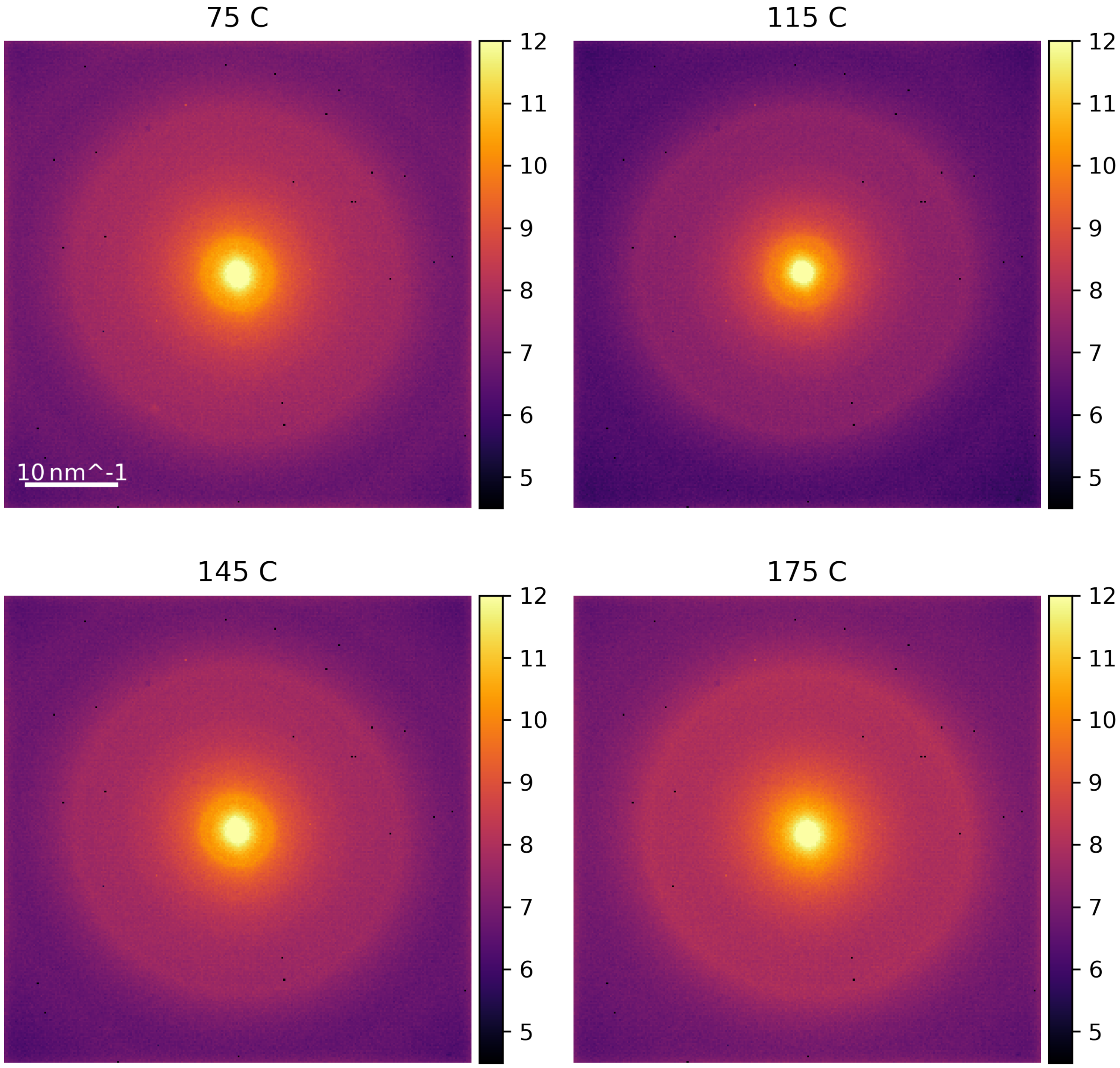

Figure 3: Integrated diffracted intensity from all pixels in 4D-STEM datasets collected from P3MEEMT annealed at various temperatures.

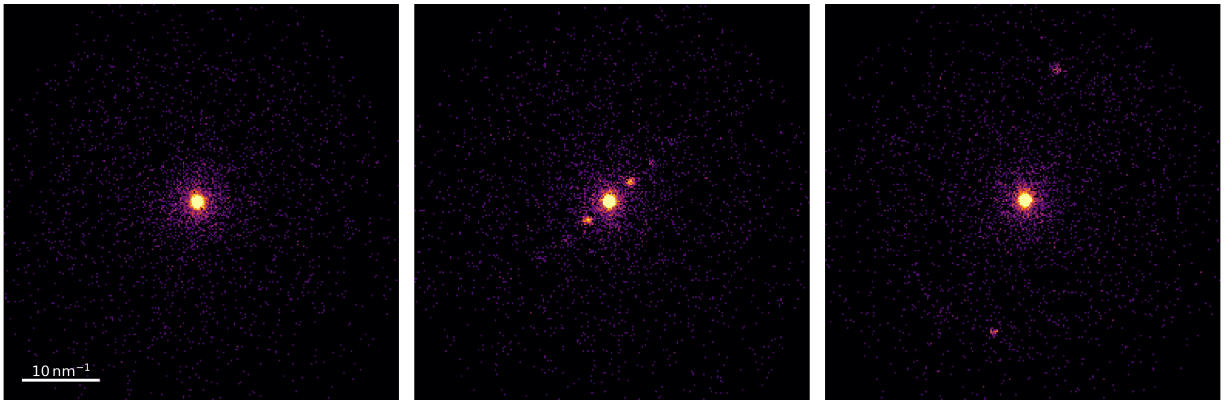

Figure 4: Examples of three classes of diffraction patterns observed in 4D-STEM of P3MEEMT film annealed at 115 °C. Patterns are typical of pixels that are amorphous or misoriented (left) or which show strong Bragg diffraction from (100) (center) or (010) oriented crystals (right). All patterns are shown in log scale.

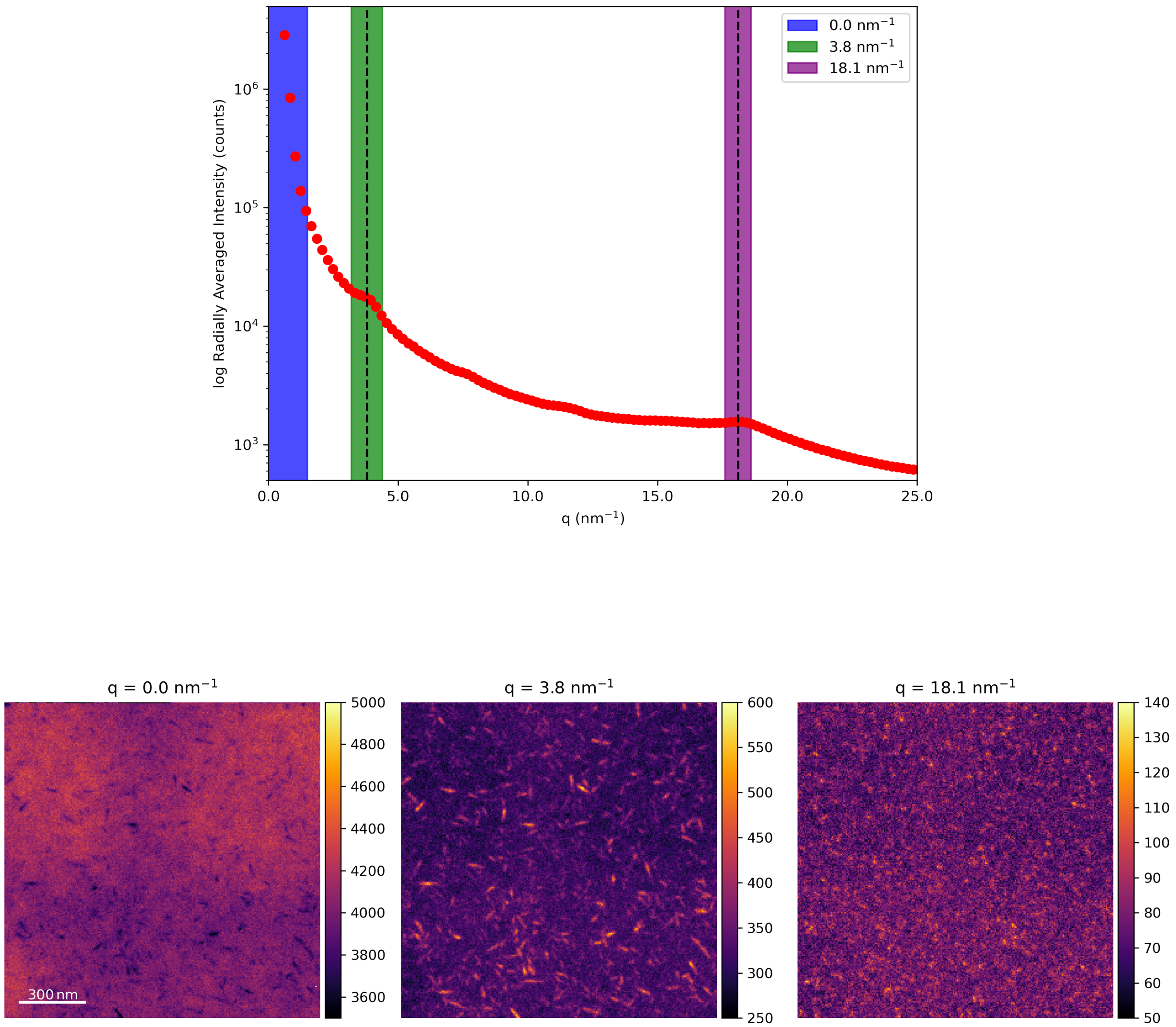

Figure 5: Radial average of sum diffraction pattern from 4D-STEM data of P3MEEMT annealed at 115 °C (top) along with virtual images (bottom) extracted from three different q ranges. The images highlight the bright-field signal (left), the (100) crystals (middle), and (010) crystals (right). For visual purposes, each image is scaled based on the intensity range.

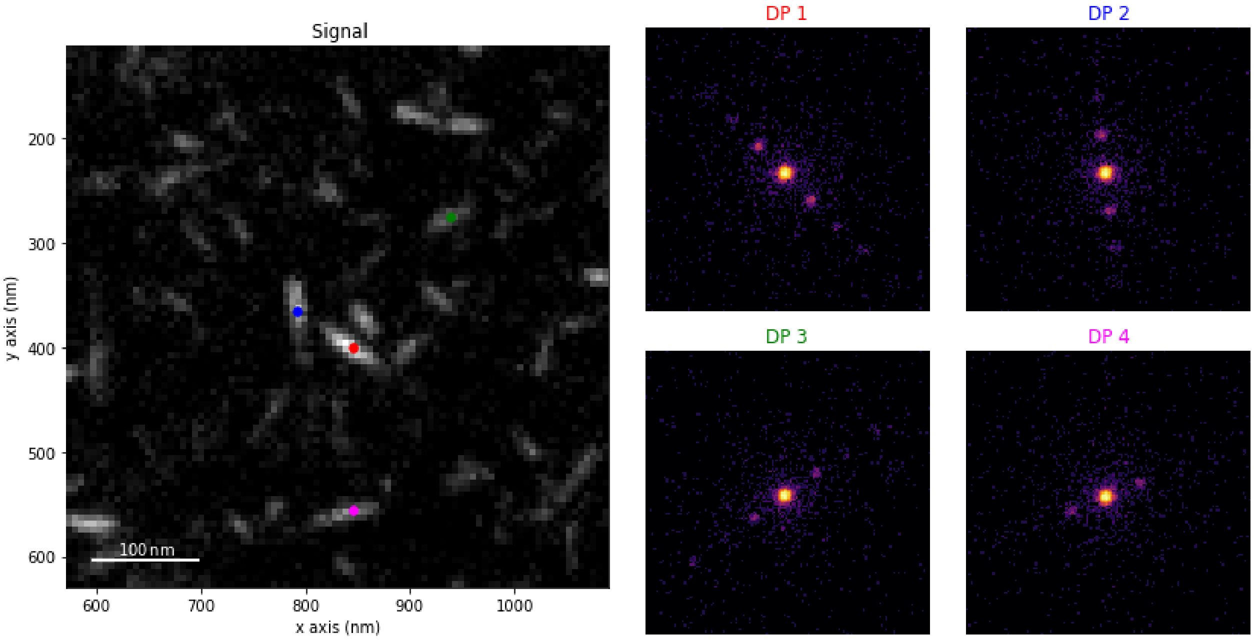

Figure 6: Virtual image formed from the (100) diffraction peak from the film annealed at 115 °C along with selected diffraction patterns extracted by indicated scan positions.

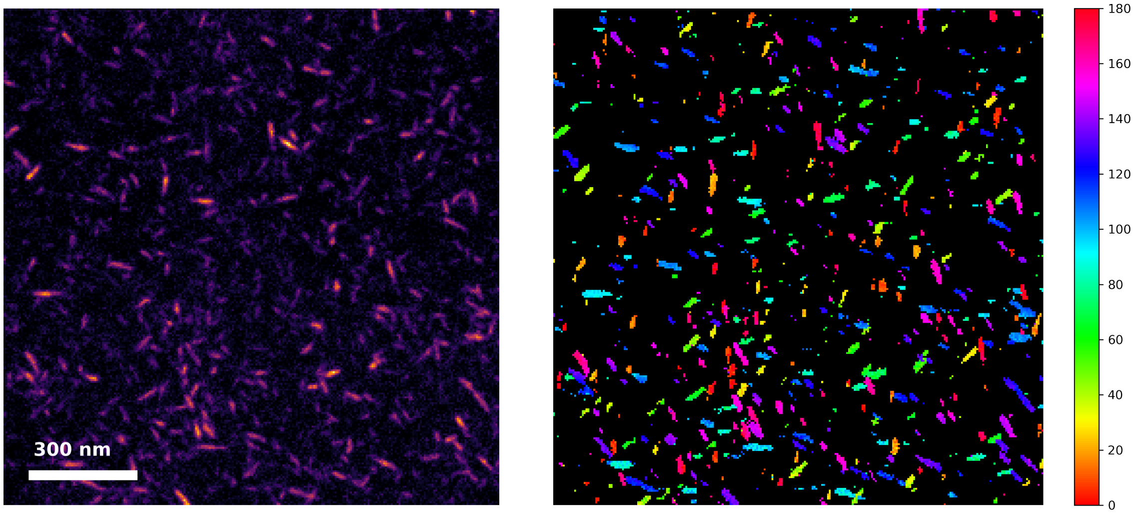

Figure 7: Virtual image formed from the (100) diffraction peak from the film annealed at 115 °C (left) along with a color map showing the orientation of crystals in the image.

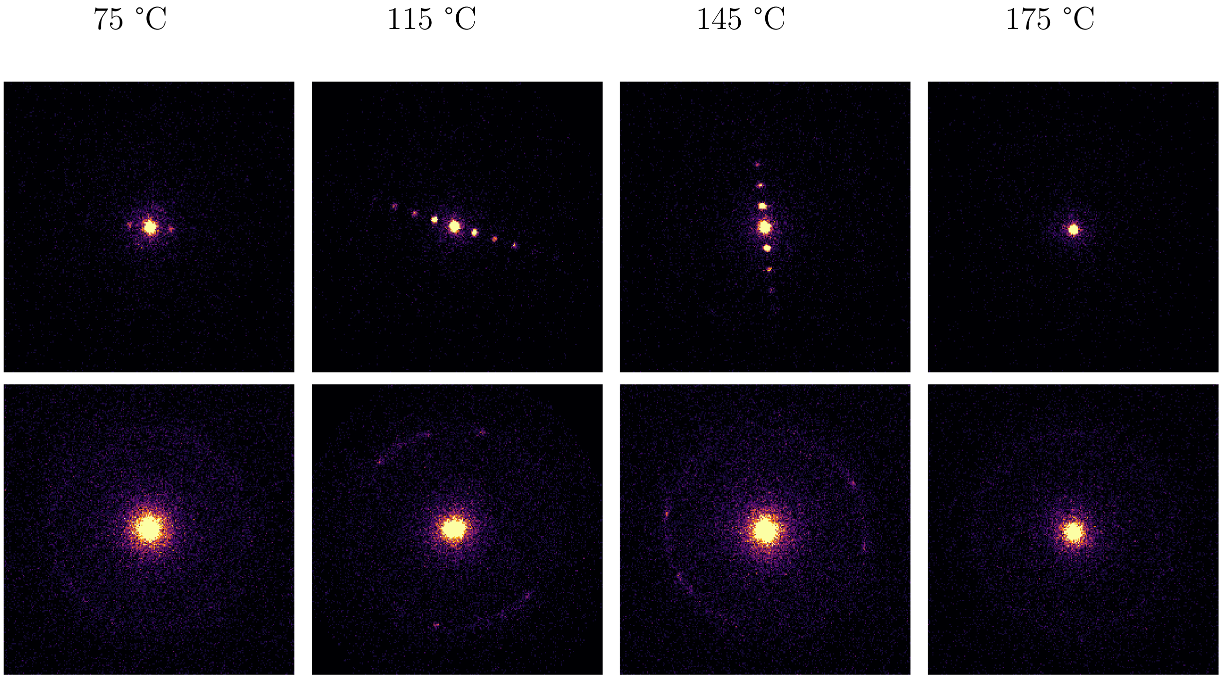

75 °C

115 °C

145 °C

175 °C

Figure 8: Diffraction patterns extracted from (100) (top row) and (010) (bottom row) oriented crystals from P3MEEMT annealed at various temperatures.

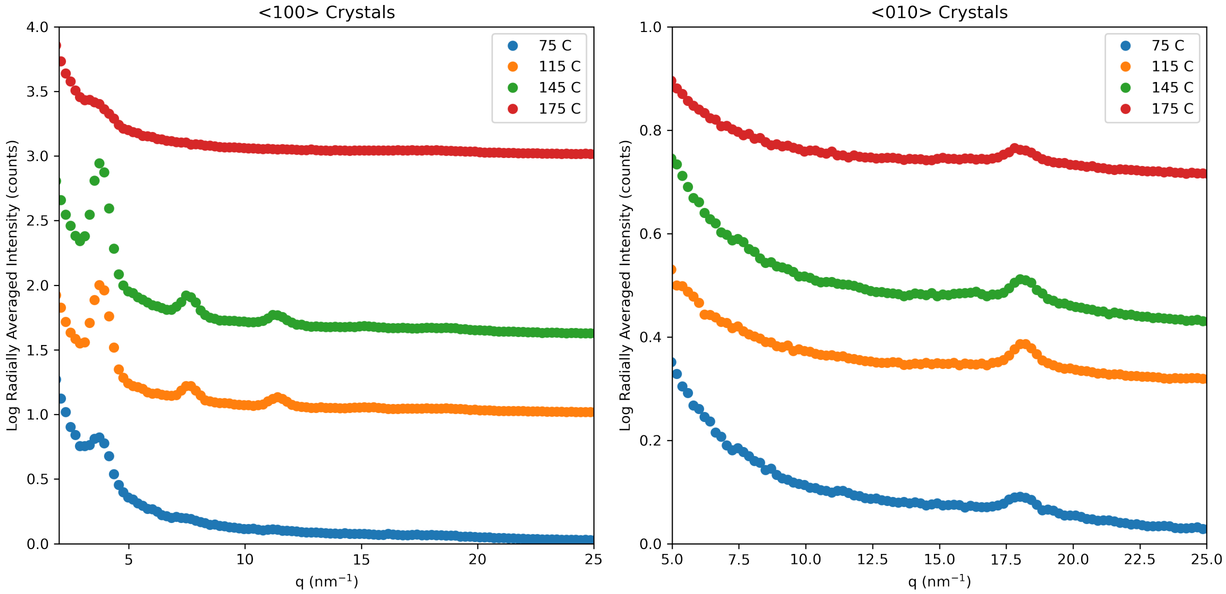

Figure 9: Radially averaged plots of most intense diffraction patterns from the (100) and (010) crystals in the P3MEEMT thermal annealing series.

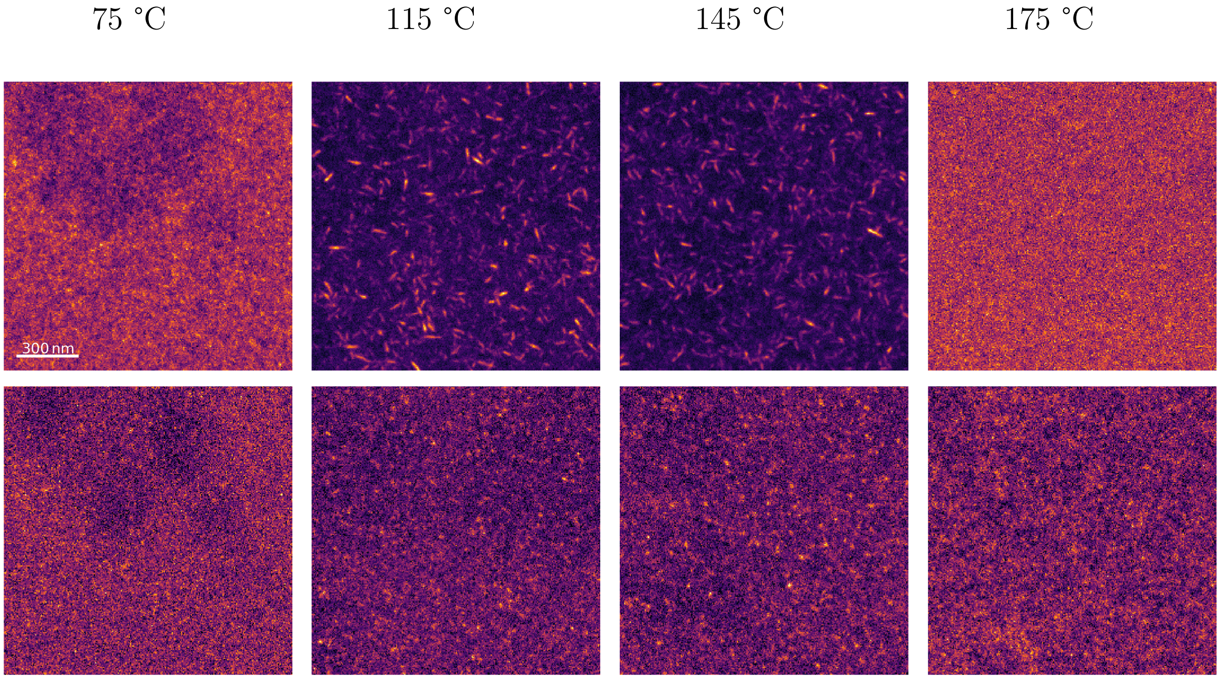

Figure 10: Virtual images extracted from the 4D-STEM datasets from P3MEEMT films annealed at various temperatures showing the (100) and (010) oriented crystals (top and bottom rows, respectively). For visual purposes, each image is scaled based on the intensity range.

TOC Graphic